Journal of Energy Storage 52 (2022) 104927

Contents lists available at ScienceDirect

Journal of Energy Storage

journal homepage: www.elsevier.com/locate/est

Research Papers

Electrodeposited poly(phenylene oxide) suppresses anodic parasitic processes in carbon-based supercapacitor electrodes operating in an aqueous electrolyte

J. M. Baptista [a,b,*], G. Gaspar [a], K.G.U. Wijayantha [b,c], K. Lobato [a]

[a] Instituto Dom Luiz, Faculdade de Ciências, Universidade de Lisboa, 1749-016 Lisboa, Portugal
[b] Energy Research Laboratory (ERL), Department of Chemistry, Loughborough University, Loughborough LE11 3TU, UK
[c] Centre for Renewable Energy Systems, Cranfield University, College Rd, Cranfield, Wharley End, Bedford MK43 0AL, UK

ARTICLE INFO

Keywords:
Supercapacitor
Aqueous electrolytes
Operational voltage
Passivation
Poly(phenylene oxide)
Electropolymerization

ABSTRACT

Aqueous electrolytes, when compared to organic electrolytes, are safer, cheaper and usually enable a higher capacitance and lower internal resistance. However, their narrow operational voltage window (ca. 1.2 V) limits the device's energy density and, as such, their current commercial use is limited. Poly(phenylene oxide) was electrodeposited on the surface of activated carbon electrodes and has been shown to decrease the anodic parasitic current. The impact on the cathodic parasitic current was minimal. Comparison of the polarisation curves obtained in 1 M Na_2SO_4 (aq) for coated and uncoated electrodes between 0.5 V and 1.1 V vs Ag|AgCl demonstrated a >66% decrease in the exchange current density of anodic processes (from 10.1 μA/cm^2 to 3.4 μA/cm^2). Assuming supercapacitor degradation is proportional to the parasitic faradaic current, this change in the anodic parameters enables a 31% increase in the upper positive potential when a maximum parasitic current density of 29 μA/cm^2 is considered acceptable. When these coated electrodes were mounted as symmetrical coin cells and operated at an increased voltage window of 1.5 V (up from 1.2 V), gains in energy and power densities were from 2.2 Wh/kg to 4.6 Wh/kg and 159 W/kg to 465 W/kg, respectively.

1. Introduction

Aqueous electrolytes, when compared to organic electrolytes, are safer, more cost-effective and environmentally friendly [1]. The smaller radii of the solvated ions is favourable for microporous electrodes and also results in electrolytes with higher conductivities [2,3]. However, because the thermodynamic potential for electrochemical water splitting is 1.23 V (at SATP), this results in a narrower operating voltage window, significantly limiting energy density [4]. When this limit is exceeded, gas evolution blocks pores, which hinders ionic transport and reduces the accessible electrode|electrolyte interface area [5]. Gao et al. [6] claimed that the maximum voltage is essentially limited by an irreversible electro-oxidation process at the positive electrode that changes the surface functional groups and generates CO and CO_2. Similarly, He et al. [5] verified, with *in situ* gas analysis, that, even when the positive electrode was polarised beyond the onset potential of the oxygen evolution reaction (OER), no O_2 evolution was observed - only CO and CO_2. This was attributed to carbon corrosion, which consumes the reactive oxygen once formed. These authors also reported that H_2 evolution on the negative electrode was only observable at -1 V vs Ag|AgCl (200 mV below the theoretical onset). This was attributed to carbon surface group modification and hydrogen adsorption.

Activated carbon is known to have high hydrogen evolution reaction (HER) overpotentials [1] and thus it can be combined, in an asymmetric configuration [7], with a positive electrode that has a high OER overpotential (e.g. MnO_2) [8]. However, despite the extended operational voltage, the performance of the device is limited to the least performing electrode and their cost can be expected to be higher [9].

Moreover, asymmetric configurations require a careful balancing of the electrode masses. This procedure is also useful in symmetric devices since one of the electrodes may more rapidly reach potentials where OER or HER initiates. This is solved by adjusting the respective electrode masses, according to Eq. (1) [10]:

$$\frac{m^+}{m^-} = \frac{C^- \Delta E^-}{C^+ \Delta E^+} \quad (1)$$

* Corresponding author at: Instituto Dom Luiz, Faculdade de Ciências, Universidade de Lisboa, 1749-016 Lisboa, Portugal.
E-mail address: jpbaptista@fc.ul.pt (J. M. Baptista).

https://doi.org/10.1016/j.est.2022.104927
Received 1 March 2022; Received in revised form 9 May 2022; Accepted 16 May 2022
Available online 2 June 2022
2352-152X/© 2022 The Authors. Published by Elsevier Ltd. This is an open access article under the CC BY-NC-ND license (http://creativecommons.org/licenses/by-nc-nd/4.0/).

where m^+ and m^- are the active masses and C^+ and C^- the specific capacitances for the positive and negative electrodes, respectively. ΔE^- and ΔE^+ are the potential differences from the potential at zero voltage (PZV) to the negative and positive potential stability limits, respectively.

Instead of balancing the mass loadings, it is also possible to relocate PZV: Yu et al. managed to do this both by amino-functionalisation of the surface [11] and also by simply applying a bias potential to the cathode [12].

The reactions that govern gas evolution depend on the availability of H^+ and OH^- and so pH neutral electrolytes are another commonly undertaken strategy [13]: Wu et al. [14] and Bichat and Piñero [15] reported voltages above 2 V for devices operating with Na_2SO_4 electrolytes (which might also be explained by the large solvation energies of Na^+ and SO_4^{2-} [13]). Fic et al. [16] further applied these ideas and achieved operating potentials of 2.1 V with a new cell design: the negative electrode in an alkaline electrolyte (KOH) and the positive electrode in an acidic (H_2SO_4) or neutral ($LiNO_3$) electrolyte. However, the system suffered from reversible electrosorption and electrolyte mixing. Instead of adapting the local availability of H^+ and OH^-, it is also possible to add redox couples to the electrolyte (or preadsorb alkali metals onto the electrode) which will compete with them, by occupying the active surface sites. However, this strategy presents various problems, such as severe self-discharge, low coulombic efficiency, high solution resistance and poor cyclability [17].

Electrolyte concentration is also an important factor, as it affects the interactions between the water molecules and solvated ions [1]. Water-in-salt electrolytes are supersaturated solutions where a solid-electrolyte interphase (SEI) is formed on the surface of the electrode and passivates it [18]. As a result, operating voltages of up to 3 V are possible [19]. However, Lannelongue et al. [20] demonstrated that the power density and cyclability were inversely correlated to electrolyte concentration. SEI formation is a common passivation mechanism that naturally occurs in Li-ion batteries [21]. However, this protective layer is rather fragile, and its dissolution is one of the main causes for thermal runaways in these devices [22]. Some electrolyte additives were found to polymerise upon cycling and form an insoluble coating that stabilises the SEI [23]. Electropolymerising a protective coating on supercapacitor electrodes can also prevent degradation in devices operating at extended voltage windows. Insulating polymers have already been electrodeposited on supercapacitor electrodes operating in organic electrolytes [24], in ionic liquids [25] and, to the best of our knowledge, there is only one report describing this strategy for aqueous electrolytes: Dong et al. [26] electropolymerised polyacrylic acid on carbon-based electrodes and the 15 nm coating managed to extend the operational voltage up to 2.4 V. However, the authors reported the performance to be affected for >15 nm-thick coatings and alerted to the importance of fine-tuning this variable. Given the high microporosity of supercapacitor-grade carbon [27], a trade-off between effectiveness of passivation and capacitance retention seems inevitable. In the present work, poly(phenylene oxide) (PPO) films were electropolymerised on activated carbon electrodes under two different conditions. Instead of a complete passivation of the electrode (which would lead to a dramatic capacitance loss), the aim was to hinder the electronic transfer between the electrode and the electrolyte and consequently extend the operational voltage whilst ensuring a good capacitance retention.

2. Experimental

2.1. Electrode fabrication

The electrodes were composed of 70 wt% activated carbon (Norit DLC Supra 50), 20 wt% of polyvinylidene fluoride (PVDF) (Merck) and 10 wt% of carbon black (Super C65, TIMCAL). To disperse the components for slurry formation, ca. 2 mL of propylene carbonate (Merck) was added for every gram of the dry mixture. The slurry was further homogenised in a three-roll mill (EXAKT 50 I) and mixed for ca. 20 min at 500 rpm and with a roll spacing of 15 μm (defining maximum particle size). With the as-obtained carbon paste, several square electrodes[1] with an area of 1 cm^2 were prepared with an automated screen-printer (ATMA, AT-45PA), using stainless steel as the substrate (Hollinbrow Precision Products, 25 cm × 30 cm, 50 μm-thick, grade 1.4310/301/$X_{10}CrNi_{18\text{-}8}$/$X_{12}CrNi_{17\text{-}7}$).

The screen (SAATI, PE AM 36.90PW) had a 190 μm mesh opening, 90 μm of nominal thread diameter and the theoretical thickness of the wet film is almost twice this value (ca. 150 μm). However, the resultant thickness of the deposited film after drying is obviously lower and depends on the slurry's solvent content. After a short drying step (120 °C in air for 10 min) a second layer was printed to fill in any faults left by the screen and to achieve higher mass loadings.[2] After the second print, the electrodes were dried overnight (120 °C in air for ca. 12 h). Finally, individual electrodes were formed by manual cutting of the screen-printed sheets.[3] A random sample of 40 electrodes was selected for mass loading measurements: the mass of the 1 cm^2 square electrodes was obtained by computing the difference between the mass of each as-prepared electrode (substrate + electrode material) and the mass of the corresponding substrate (i.e. after removing the electrode material). The average mass loading was found to be 5.1 ± 0.7 mg/cm^2 (1σ).

The remaining electrodes were electrochemically characterized (as described below) and then carefully washed with deionised Millipore water (18.2 MΩ) and dried (100 °C in air for ca. 1 h). The electrodes were distributed in groups of 5. Each group was composed to maximise the standard deviation among the capacitances of its elements whilst ensuring that the difference in average capacitance of the groups was minimised. In total, there were 12 groups: 4 were kept "uncoated" (Unc. A, Unc. B, Unc. C and Unc. D), 4 were electropolymerised at 1.15 V vs Ag pseudo-reference (P115A, P115B, P115C and P115D) and the electrodes of the remaining 4 groups were electropolymerised at 1.5 V (P150A, P150B, P150C and P150D).

2.2. Electropolymerisation

The electropolymerisation procedure was adapted from Deheryan et al. [28]. The electropolymerising solution contained 50 mM of phenol, 50 mM of TMAH·$5H_2O$ and 100 mM of TBAP in acetonitrile. TBAP and TMAH·$5H_2O$ were first weighed in an Ar-filled glovebox (O_2 < 1%) and mixed with molecular sieve-dried acetonitrile (HPLC grade). TMAH·$5H_2O$ is poorly soluble in acetonitrile and thus requires a long (ca. 1 h) mixing step at ca. 70 °C. To minimise spontaneous polymerisation, phenol was only added after this mixing step and after cooling the solution down to room temperature. Since the solution was transferred to a sealed container, N_2 was bubbled for ca. 5 min into the solution to expel the residual oxygen dissolved in it and then a constant flow of N_2 was kept during electropolymerisation. The electropolymerisations were carried out in a 3-electrode configuration, where the CE was a Pt mesh, the WE was the activated carbon electrode and the RE was an Ag wire (i.e. it was a quasi-reference electrode). The quasi-reference electrode was used instead of a conventional Ag|AgCl to avoid the blockage of the electrode's frit and to prevent the contamination of the solution with AgCl. The electrodeposition was controlled by a Solartron 1260 potentiostat, run by a PowerSuite software. Electrodeposition was potentiostatic at either 1.15 V or 1.5 V, for 100 s (henceforth designated set of conditions P115 and P150, respectively). After electropolymerisation, each electrode was dipped in an

[1] Rectangular electrodes were also printed for the coin cells (16 mm electrode diameter).

[2] High mass loadings enable higher energy densities both in supercapacitors and in Li-ion batteries [43].

[3] A portion of the coated stainless steel was left bare to enable the connection to a crocodile clip for 3-electrode electrochemical measurements.

acetonitrile-filled beaker for ca. 2 min, then transferred to a new acetonitrile beaker and finally it was carefully rinsed with Millipore deionised water. The 5 electrodes from a same group were consecutively electropolymerised in the same solution. A fresh solution was prepared for each group. After the rinsing steps, the electrodes were dried (100 °C in air for ca. 1 h).

2.3. Electrochemical measurements

The electrochemical measurements were performed with an Autolab PGSTAT302N (Metrohm) operated with NOVA 2.1 software. The electrodes were submersed in aqueous solutions of Na_2SO_4 (1 M), in a 3-electrode setup using an Ag|AgCl (3 M) reference electrode and a mixed metal oxide-coated titanium counter electrode (De Nora). For the working electrode, the stainless-steel substrate was masked with Kapton tape (*vd* Fig. 1) to prevent its direct exposure to the electrolyte.

All the electrochemical measurements initiated with a preliminary performance assessment consisting of 60 wetting cycles (which were enough to stabilise the electrode) performed at 30 mV/s between −0.4 V and 0.5 V. Next, 6 of the 12 groups of electrodes (Unc. C, Unc. D, P115C, P115D, P150C and P150D) were tested within this same range at varying scan rates (10, 20, 30, 40, 50, 60 and 75 mV/s) and then galvanostatic charge-discharge tests were carried out (also from −0.4 V to 0.5 V) at several current densities (1–8 mA/cm^2). Only the 10th voltammogram/charge-discharge cycle was considered for calculations. Finally, to investigate the impact of the coating on the ionic diffusion, the electrodes were also characterised by potentiostatic electrochemical impedance spectroscopy, at 0 V, with a 10 mV amplitude, from 500 kHz to 40 mHz. This general characterisation procedure was then repeated for increasingly wider potential windows. Unc. D, P115D and P150D were tested in a widening negative bias window, increasing progressively (−0.4 V, −0.5 V, −0.6 V, −0.7 V, −0.8 V, −0.9 V, −1.0 V and −1.1 V). The other 3 analogous groups (Unc. C, P115C and P150C) were tested in a widening positive bias window, increasing progressively (0.5 V, 0.6 V, 0.7 V, 0.8 V, 0.9 V, 1 V and 1.1 V). The complete large dataset can be made available upon request.

The specific capacitance (C_{sp}), the energy density (E_{sp}) and power density (P_{sp}) were obtained from galvanostatic charge-discharge tests and calculated, respectively, via Eqs. (2), (3) and (4) [29]:

$$C_{sp}[\mathrm{F/g}] = \frac{i\,(t_f - t_0)}{[V(t_f) - V(t_0)]\,m} \tag{2}$$

$$E_{sp}[\mathrm{Wh/kg}] = \frac{0.5\,C_{sp}\,[V(t_f) - V(t_0)]^2}{3.6} \tag{3}$$

$$P_{sp}\,[kW/\mathrm{kg}] = \frac{3.6\,E_{sp}}{t_f - t_0} \tag{4}$$

where, t_0 and t_f are, respectively, the time at the start and end of the discharge, i is the (constant) value of the current, $V(t_f)$ and $V(t_0)$ are, respectively, the potential at the end and at the start (i.e., after the initial IR drop) of the discharge, and m is the electrode mass (in g).

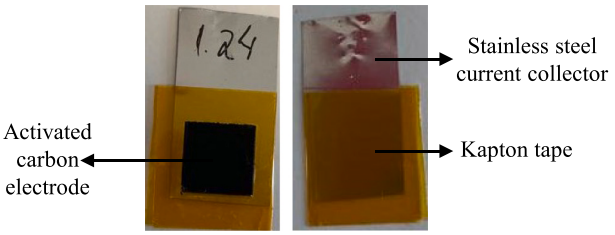


Fig. 1. Front and back view of an electrode, showing how the regions of stainless steel that were to be submerged in the electrolyte were fully covered with Kapton tape.

A final set of six group of electrodes were not assessed for performance but were used to test polymer passivation effectiveness. In order to only assess the faradaic currents and hence minimise capacitive currents, linear scanning voltammetry was performed at 42 μV/s. Three groups of electrodes were tested in the negative range (from 0 to −1.1 V), and another three groups in the positive range (from 0 to 1.1 V).

Table 1 summarises the electrode groups that were used for each measurement.

Electrodes were also tested in a 2-electrode coin cell setup (CR2032 coin cells, 16 mm diameter electrodes soaked in 1 M Na_2SO_4 aq). After 60 wetting cycles at 30 mV/s, the cells were tested at varying scan rates (10, 20, 30, 40, 50, 60 and 75 mV/s) and then galvanostatic charge-discharge tests were carried out at several current densities (0.1–1.5 A/g) up to 1.9V. Using a BTS4000-5V10mA battery tester (Neware), stability was assessed for 10,000 cycles at 0.2 A/g charge/discharge currents.

2.4. XPS analysis

The surface compositions of the coated and uncoated samples were measured through X-ray Photoelectron Spectroscopy (XPS) analysis using a Thermo Scientific K-Alpha X-ray Photoelectron Spectrometer equipped with a monochromatic Al Kα X-ray source. The excitation sampling spot size was 400 μm, and the high-resolution spectra were collected with 0.1 eV spectral resolution. The spectra were deconvoluted using the Avantage software whilst the elemental concentration quantification was applied using standard single element sensitivity factors.

3. Results and discussion

Fig. 2 shows the average evolution of the current density on carbon-based electrodes during the potentiostatic electropolymerisations P115 and P150.

As the electrodeposition progresses, the current density through the electrode experiences an exponential decrease (from 8.9 to 4.4 mA/cm^2 and from 18.2 - to 3.7 mA/cm^2), which suggests the presence of an electrically insulating film. Also, for curve P150, the rate of decay is ca. 3 times larger than for P115, suggesting that the growth of poly(phenylene oxide) is accelerated at higher potentials. If given enough time, the current density would reduce several orders of magnitude, but, in preliminary studies, this was found to have a detrimental effect on the capacitance. It is worth keeping in mind that, in supercapacitor electrodes, the capacitance arises mostly from micropores (<2 nm) [30] and thus even a very thin polymer layer can be expected to block these, resulting in unacceptably degraded performance. As such, instead of aiming at a full passivation of the electrodes, the goal was to reach a compromise between capacitance and extended operational potential.

Fig. 3a) and b) shows the voltammograms of electrodes before and after the electrodeposition. As expected, the absence of redox peaks in the coated electrodes demonstrates that PPO did not introduce any pseudocapacitance, unlike conducting polymers and transition metal oxides or nitrides [31]. Also, for a same electrode, there is a significant decrease in the capacitance after electropolymerisation and it is more pronounced for P150 electrodes (only 53% of capacitance retention) than for P115 electrodes (65% of capacitance retention), which indicates that electropolymerising at higher potentials promotes a broader

Table 1
Summary of groups used for the various measurements.

	Positive range 0 to 1.1 V	Negative range 0 to −1.1 V
Polarisation measurements to assess passivation	Unc. A, P115A, P150A	Unc. B, P115B, P150B
General performance measurements for increasing potential windows	Unc. C, P115C, P150C	Unc. D, P115D, P150D

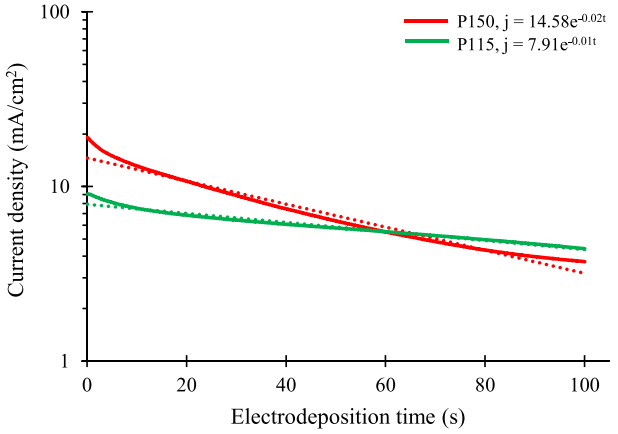


Fig. 2. Potentiostatic electrodeposition curves obtained in the organic solution detailed in Section 2.2, at 1.15 V vs Ag pseudo-reference (P115) and at 1.5 V vs Ag pseudo-reference (P150) - average curves obtained for 5 electrodes. The trendlines (dotted) were obtained using a least squares fitting.

electrode surface coverage.

The coating also has an impact on the Nyquist plots, as shown in Fig. 3c) and d), where a ca. 3-fold increase in the semi-circle's diameter is visible between the uncoated and the coated electrodes. This increase in the charge transport resistance (from 15 Ω to 42 Ω and to 47 Ω) is likely due to the polymer blocking a few regions of the electrode, hence hindering the electrolyte's access to some of the pores.

To facilitate XPS analysis, electrodeposited polymer films on bare stainless-steel were also evaluated. Results for stainless-steel are shown in Fig. 4. Comparisons to polymer-coated activated carbon electrodes are shown in Figs. 5 and 6.

One of the most striking differences between the bare and polymer-coated stainless steel is the abundance of C-O-C (at ca. 286 eV): whilst it appears to be only residual in the former (5% of the C1s peak), it experiences a six-fold increase on the latter, as shown in Fig. 4a) and b). This is unsurprising, given that C-O-C bonds correspond to chain propagation within PPO [32]. Other obvious differences, shown in Fig. 4c) and d), include the sharp decrease – from 19% to 1.5% and from 23% to 3%, respectively- in the O1s contents of chromium oxides and hydroxides (which protect the steel from corrosion [33]). This suggests that this original layer was mostly covered. It is also interesting to note that the relative abundance of C-OH increased from 4% to 12%: whilst the pre-coating amount was likely due to cleaning residues (from ethanol), the C-OH in the polymer-coated stainless steel suggests the presence of some unreacted phenol monomers (also rich in C-OH) which might have got trapped in the coating.

Because PPO contains the same bonds that can be found at the surface of the activated carbon [34], the presence of PPO by XPS analysis is not indisputable. Nonetheless, as shown in Fig. 5c) and d), the relative abundance of C-O-C in the C1s peak increased from the uncoated sample (19.6%) to the P115 sample (22.2%) and even slightly more when compared to the P150 sample (22.8%).

To evaluate PPO heterogeneity, each electrode was XPS-mapped and the average atomic percentage of oxygen was calculated. Although the peak shown in Fig. 5a) – corresponding to a single spot – does not show a significant variation between the amplitudes of the O1s envelopes for different electrodes, the averaged atomic percentage of oxygen was found to be higher for the P115 (4.7%) and for the P150 (6.5%) electrodes than for the uncoated electrode (4.1%), as represented in Fig. 5b). This fact can also be observed in the maps shown in Fig. 6a), b) and c). This is consistent with the fact that the theoretical oxygen content in PPO is 11% [35] whilst the oxygen content of the used activated carbon is <3% [27]. Because the oxygen content does not increase 4-fold for the electrodeposited surfaces, one can argue that the polymer is only covering parts of the surface.

Also noteworthy is the fact that, not only Fig. 6d) and g) but also Fig. 6e) and h), and f) and i) seem to be almost complementary to each other. The observation that the fluoride-rich regions correspond, in all samples, to regions with a lower amount of carbon (and vice versa) suggests that the polymer was not electrodeposited on PVDF-rich areas. This is consistent with the insulating nature of this binder [36].

To test the effectiveness of the passivation, polarisation curves were obtained via linear scan voltammetries performed at a very low rate (42 μV/s), as shown in Fig. 7. The assumption here is that the extent of the degradation reactions is proportional to the current density of these

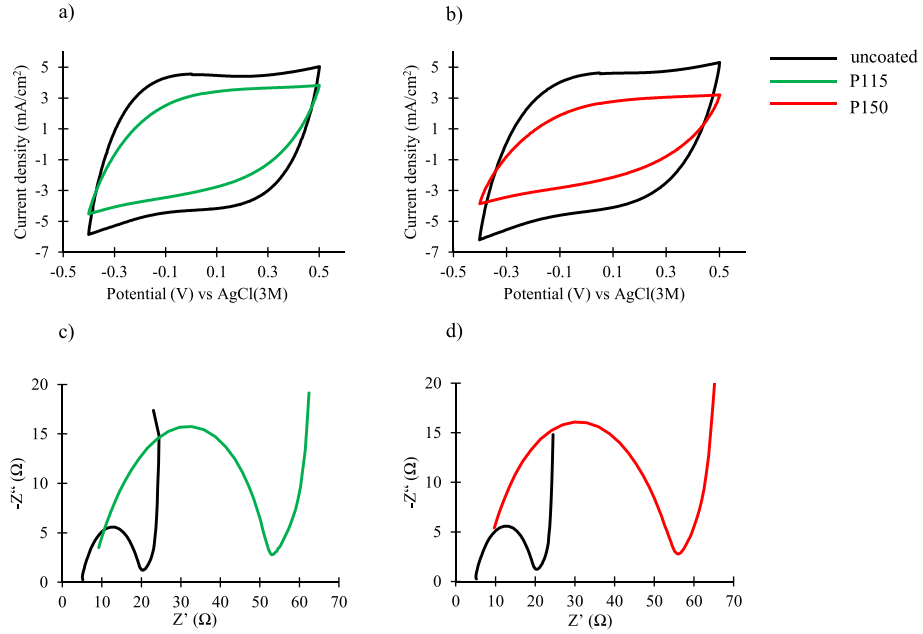


Fig. 3. Voltammograms recorded in Na_2SO_4 (1 M) at 30 mV/s before and after electropolymerisation at 1.15 V - P115 (a) – and at 1.5 V - P150 (b). Nyquist plots obtained for uncoated electrodes and for P115 (c) and for P150-coated electrodes (d). These 3-electrode measurements correspond to the electrodes whose behaviour was the most similar to that of the average behaviour of the group.

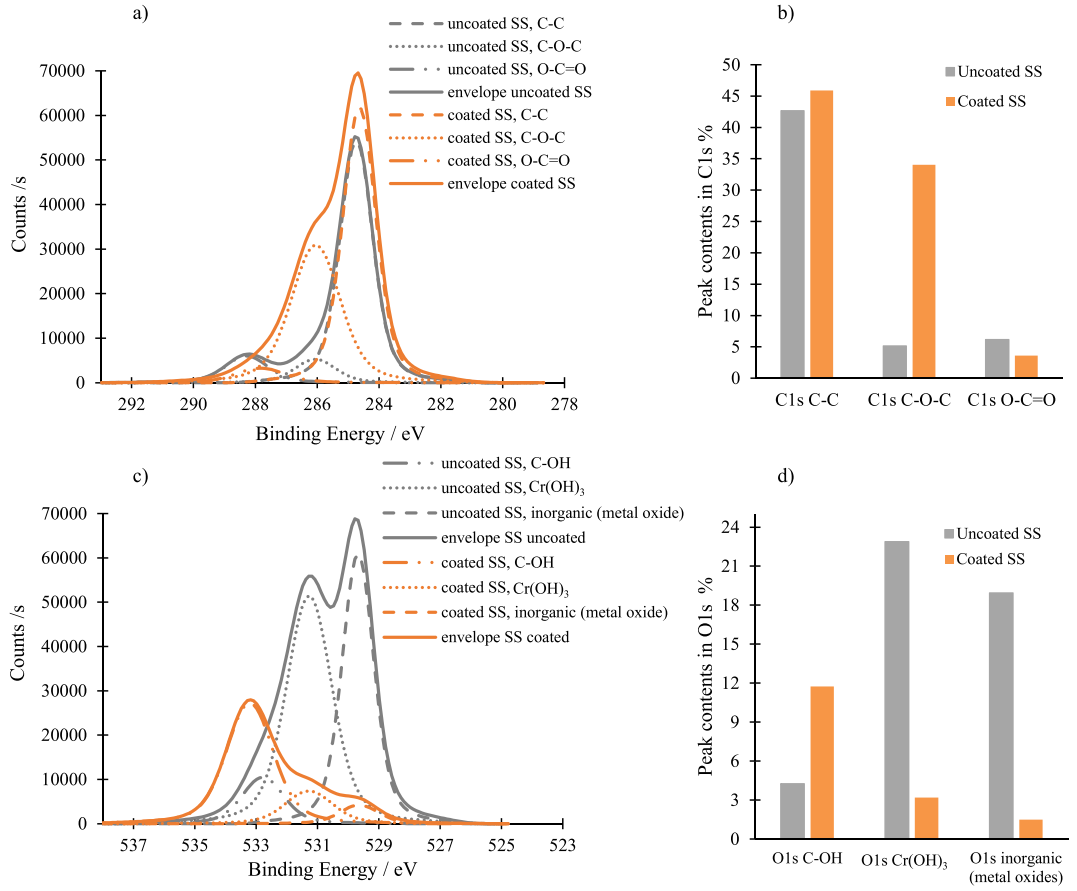


Fig. 4. Deconvoluted XPS peaks C1s (a) and O1s (c) and relative abundance of bonds deconvoluted from C1s and O1s peaks (b and d, respectively) in uncoated stainless steel and in polymer-coated stainless steel.

parasitic faradaic reactions [37]. As such, if a higher overpotential is required to achieve the same parasitic current density, it means that a wider potential range can be applied without any additional degradation.

Fig. 7 shows that the current density increases exponentially with the overpotential and can be modelled with Eq. (5).

$$j = j_0 e^{\eta/\beta} \tag{5}$$

where j and j_0 are, respectively, the current density and the exchange current density; β is the Tafel coefficient [37] and η is the overpotential at which the anodic/cathodic reaction is taking place. Linearising the equation, we obtain Eq. (6),

$$logj = \frac{loge}{\beta}\,\eta + logj_0 \tag{6}$$

where the term $\frac{loge}{\beta}$ is the slope of the curve (proportional to the charge transfer coefficient [38]) and the term log(j_0) is the y-axis intercept.

Fig. 7 shows that the cathodic parasitic currents remained unaffected by the passivating coating (the exchange current density only decreased from 26.3 μA/cm^2 to 20.4 μA/cm^2 and to 23.0 μA/cm^2). One possible explanation is that the non-uniform coverage of the surface of the coated electrodes and the small ionic radius of hydrated Na^+ (only 0.36 nm, whilst hydrated SO_4^{-2} has 0.73 nm [13]) enabled their penetration through the polymer's pinholes. On the other hand, since the cathodic parasitic currents have a much lower slope, their unsuccessful suppression seems to be less problematic – i.e. even a large increase in the overpotential causes only a modest increase in the cathodic current. This behaviour might be explained by the reversible adsorption of nascent hydrogen onto the negatively polarised electrode. In non-acidic electrolytes, the formation of CH_{ad} (the intermediate step that precedes HER) was shown to be the main reaction taking place down to −1.6 V vs Ag|AgCl. This means that the additional polarisation energy was being mostly used to further diffuse the adsorbed hydrogen into the bulk of the carbon host, occupying sites with higher adsorbing energy [39]. It is thus the anodic parasitic reaction (most likely carbon corrosion) that seems to be the governing gas evolution process (and thus the main driver for degradation) [5,6], and here, the coating clearly caused an impact. Even though the slope remained essentially the same, the exchange current density decreased significantly (from 10.1 μA/cm^2 to 4.3 μA/cm^2 and to 3.4 μA/cm^2), which suggests a lower electron transfer rate between the electrode and the electrolyte and thus a higher reaction energy barrier [40]. This means that, to achieve the same parasitic current density, a higher overpotential is required, which, in practice, translates into an increase in the stable upper potential. Shown in Fig. 8 are cyclic voltammetries where the maximum positive potential was progressively increased.

Although the coated electrodes (Fig. 8b)) display smaller capacitances for narrower potential ranges, their capacitance increases more rapidly with increasing potential ranges and thus the performance differences decrease (see Fig. S5). For example, when P115 electrodes are cycled up to 1 V, their average capacitance is 43 F/g (for uncoated electrodes tested in the same conditions, the average capacitance is 44 F/g). Also, it is noteworthy that, for P115 electrodes, the voltammograms remain stable up to a very high potential of 1.1 V. On the contrary, uncoated electrodes show signs of degradation (a narrower and noisy voltammogram that hints at gas evolution and consequent fluctuations of the available active area) when cycled up to 1.1 V (Fig. 8a)).

Nonetheless, milder degradation processes can often go unnoticed in the first few voltammograms and only become evident upon long-term

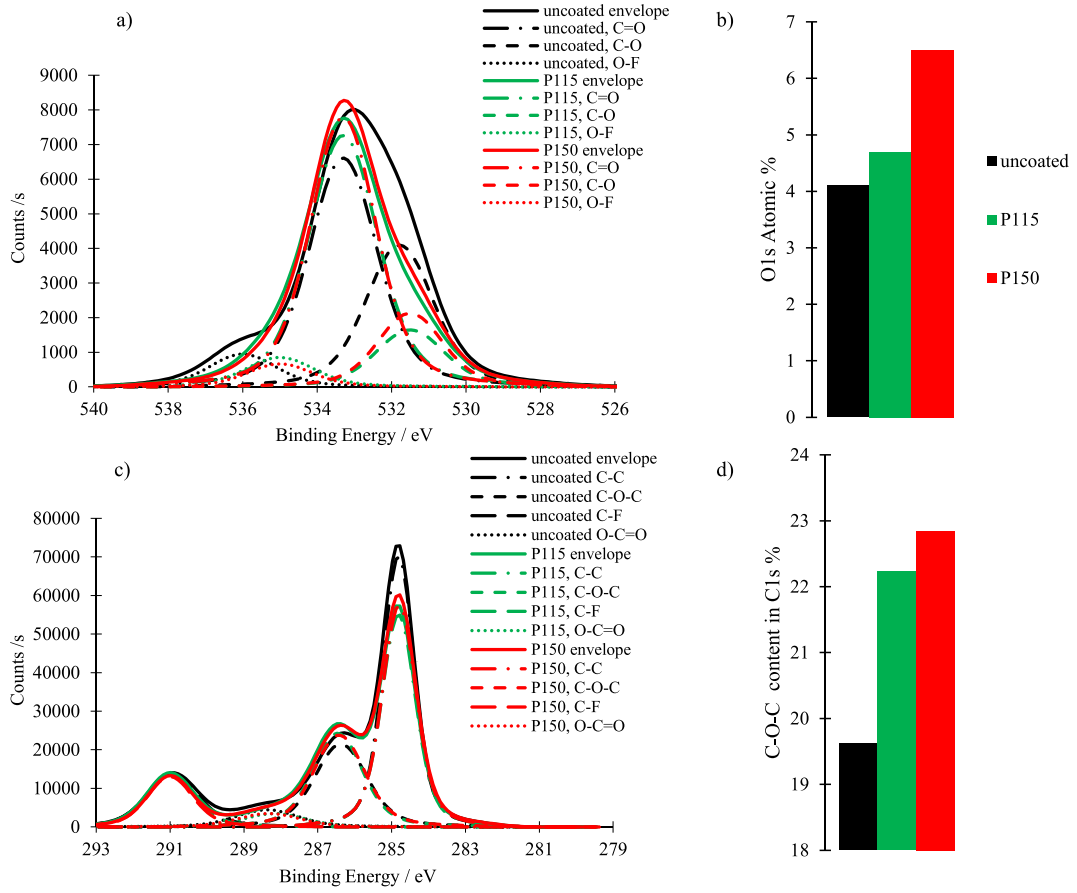


Fig. 5. Deconvoluted XPS peaks O1s (a) and C1s (c), average atomic percentage of O1s obtained from the maps shown in Fig. 6 (b) and relative abundance of C-O-C in the C1s peak, for uncoated (black), P115- (green) and P150-coated (red) electrodes. Figs. S2 and S3 show, respectively, the O1s and C1s peaks separated for each electrode. (For interpretation of the references to colour in this figure legend, the reader is referred to the web version of this article.)

cycling [41]. Since supercapacitors are expected to remain stable for $>10^5$ cycles, their cyclability should ideally be tested for each voltage window in order to define the adequate operational range. However, this method is time-consuming and thus, estimating the available cell voltage based on the anodic and cathodic polarisation curves can be a better starting point. Fig. 9 shows the maximum available cell voltage as a function of the acceptable parasitic current (Eq. (7), which was obtained by adapting Eq. (6) to the positive and negative electrodes and then inverting and combining the resulting equations).

$$\Delta V_{max} = \Delta V_0 + \frac{\beta_a}{loge} log\left(\frac{j_{max}}{j_{0,a}}\right) + \frac{\beta_c}{loge} log\left(\frac{j_{max}}{j_{0,c}}\right) \quad (7)$$

where ΔV_0 is the theoretical cell voltage at equilibrium; j_{max} is the maximum current density considered acceptable (which will be the same for the positive and negative electrodes, unless they have different areas or mass loadings); $j_{0,\,a}$ and $j_{0,\,c}$ are, respectively, the exchange current density for the anodic and for the cathodic parasitic reactions; and β_a and β_c are, respectively, the Tafel coefficients for the anodic and for the cathodic parasitic reactions.

Determining the "onset potential" for degradation is not a straightforward task. However, assuming one starts by defining an acceptable value for the parasitic current, it then enables the determination of the stable potential window for each electrode and, consequently, of the available cell voltage. As represented in Fig. 9, the theoretically available cell voltage increases with the value of the parasitic current considered "acceptable" and the rate of increase is very similar between the uncoated and the coated electrodes. In agreement with the observations made for Fig. 7, the main difference is the y-intercept: for a same acceptable parasitic current, the available cell voltage is higher for the coated than for the uncoated electrodes (despite the considerably large spread of results obtained for these).

The choice of the acceptable parasitic current will inevitably affect the cyclability of the cell: the higher the tolerance given to the former, the larger the impact on the latter due to accelerated degradation. However, in some applications, it might be worth sacrificing some cyclability to gain energy density. Two different scenarios – corresponding to two different "acceptable" current densities, based on the calculations shown in Fig. 9 were studied for symmetric coin cells fabricated with uncoated electrodes and with P115- and P150-coated electrodes. The respective Ragone plots are displayed in Fig. 10:

For uncoated electrodes, a parasitic current density of 29 μA/cm^2 should correspond to a stability window of 1.2 V, whilst, for coated electrodes (regardless of the electropolymerisation potential), this same current should enable a maximum voltage of 1.5 V and, for a current density of 47 μA/cm^2, the stability window was 1.7 V for the uncoated cells and 1.9 V for the coated cells. The Ragone plots shown in Fig. 10 suggest that, for the cells fabricated with the coated electrodes, the energy and power densities obtained for a same parasitic current density are higher (e.g. for 29 μA/cm^2, their values are 4.0 Wh/kg and 4.6 Wh/kg, compared to 2.2 Wh/kg and 345 W/kg and 465 W/kg, compared to 159 W/kg). This observation is not trivial, because, given the capacitance loss initially demonstrated for a narrow potential window (around 40% - see Fig. 3), the voltage gains shown here (12 and 25%) should not be enough to compensate it and yet they do. This is likely explained by the phenomenon observed in Fig. 8. In short: the passivating coating might block a few pores but also enables a stable operation at higher potentials, which in turn increases the capacitance by facilitating

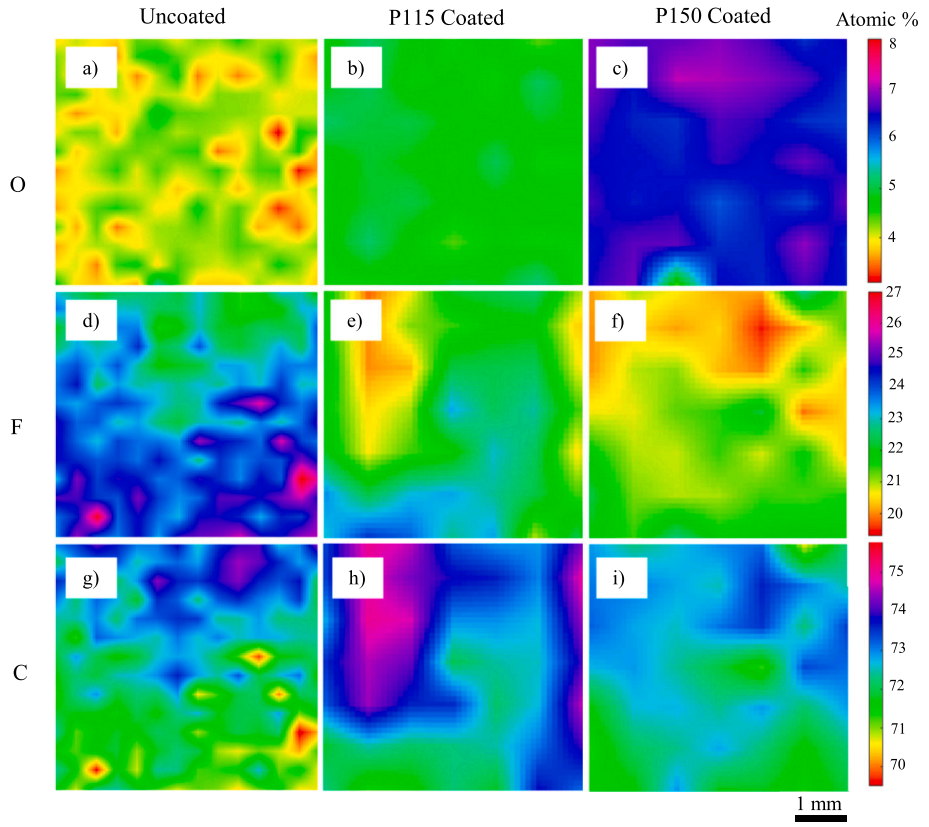


Fig. 6. Maps showing the relative abundance of oxygen (a, b, c), fluoride (d, e, f) and carbon (g, h, i) in an uncoated activated carbon electrode (a, d, g), in a P115-coated electrode (b, e, h) and in a P150-coated electrode (c, f, i). The colour bar is the same for each row (i.e. for each element). (For interpretation of the references to colour in this figure legend, the reader is referred to the web version of this article.)

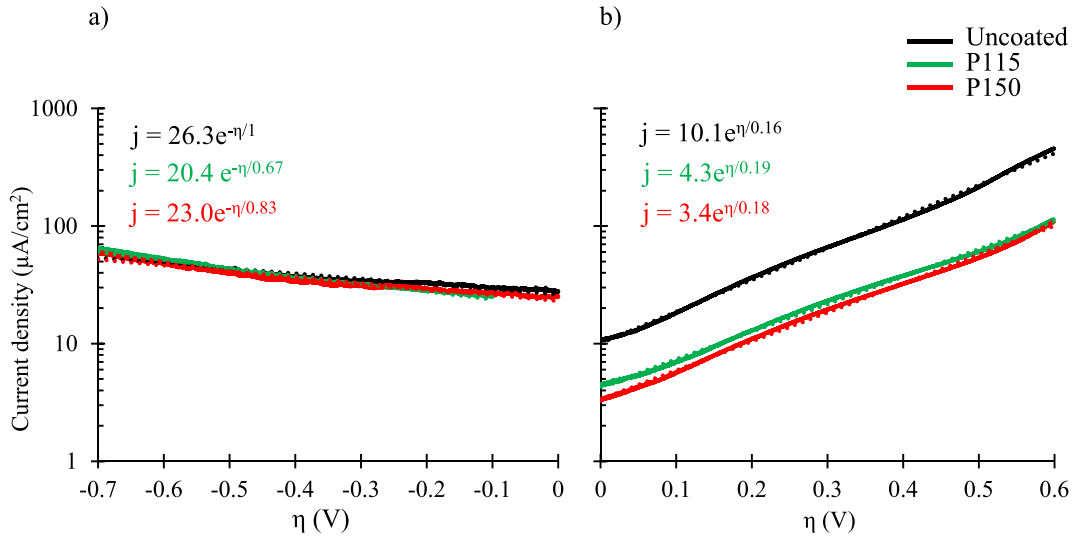


Fig. 7. Cathodic (a) and anodic (b) Tafel plots obtained for uncoated electrodes and for P115- and P150-coated electrodes (linear regions – i.e., where the current density varies exponentially with the overpotential). In a), η is the difference between the applied potential and −0.4 V and in b), η is the difference between the applied potential and 0.5 V. Data obtained at 42 μV/s.

electrolyte diffusion into more restricted pores (possibly due to partial desolvation [42]). Reversible hydrogen storage at the negative electrode might have contributed to the capacitance enhancement as well [5,6]. Both the enhanced capacitance and the increased maximum voltage translate into a better device performance.

The cyclability measurements shown in Fig. 11 suggest that the cells fabricated with PPO-coated electrodes do not degrade faster than the cells fabricated with uncoated electrodes during the 10,000 cycles up to 1.9 V. However, it is also not clear that the degradation is slower than for the uncoated cells. The two reference (uncoated) cells show very distinct behaviours: one degrades quickly and, afterwards, seems to stabilise whilst the other experiences a lower initial decay but then starts failing abruptly at about 8000 cycles. This means that other important factors are clouding the conclusions about the long-term performance of the

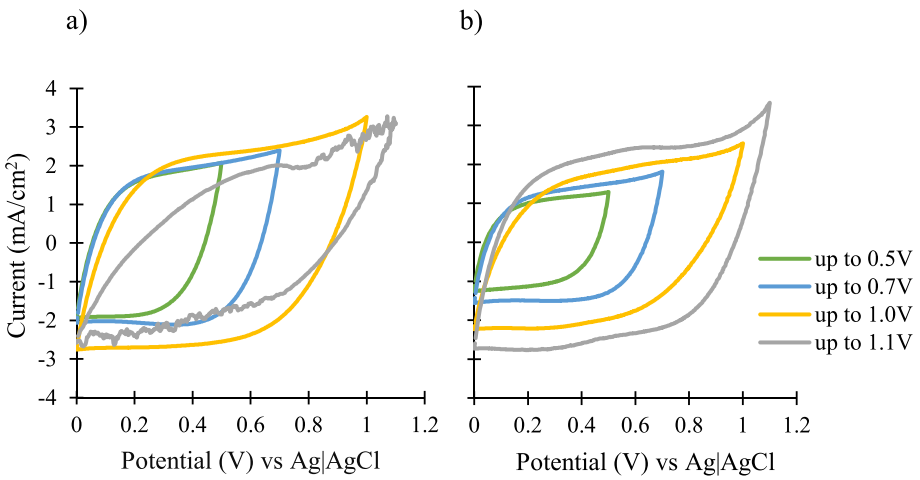


Fig. 8. Voltammograms recorded at 10 mV/s, within the positive potential ranges, at increasing upper potentials, for an uncoated electrode (a) and for a P150 electrode (b). Each one of the depicted voltammograms has been obtained after 10 cycles within the designated potential range. Fig. S4 shows the coated and uncoated voltammograms in the same plot, for each potential range.

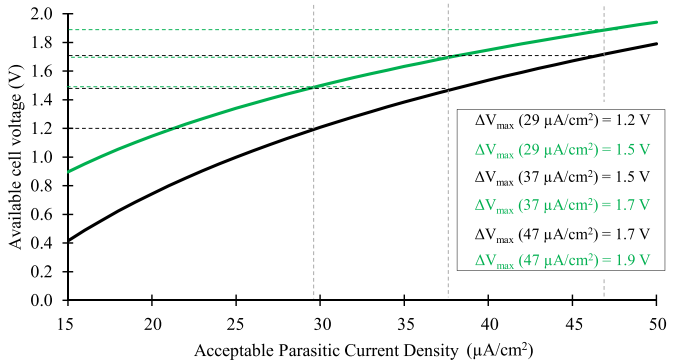


Fig. 9. Theoretically available cell voltage for uncoated electrodes and for P115-coated electrodes, depending on the value of the polarisation current that is considered acceptable.

cells. One of them is likely related to charge balancing issues (already explained in Introduction). Even when electrodes with different mass loadings are combined to ensure that their stability window is respected, these efforts can be undermined by the fact that the capacitance will change along the cycles - and not necessarily in the same way for both electrodes. The only way to individually assess the ageing of each electrode would be to insert a pseudo-reference electrode between them (which brings additional challenges).

Although the PPO coating aims to decrease the extent of voltage-driven degradation reactions it will never eliminate these completely. The fact that this happens within porous electrodes inside a sealed and pressurised container adds another layer of complexity to the problem and contributes to an increased variability among the ageing profiles. The possibly stochastic ageing nature requires carefully designed experiments to ensure that large variability between samples is taken into account.

4. Conclusions

An insulating polymer (PPO) has been potentiostatically electrodeposited at 1.15 V and at 1.5 V vs Ag pseudo-reference on carbon-based supercapacitor electrodes. The comparison of polarisation curves obtained for coated and uncoated electrodes in aqueous solutions of Na_2SO_4 revealed that the anodic exchange current density was significantly lower (4.3 μA/cm^2 and 3.4 μA/cm^2 compared to 10.1 μA/cm^2) for the passivated samples. Assuming that the anodic current density is directly related to the degradation reactions that take place at more positive potentials (possibly OER and/or CO and CO_2 evolution), having

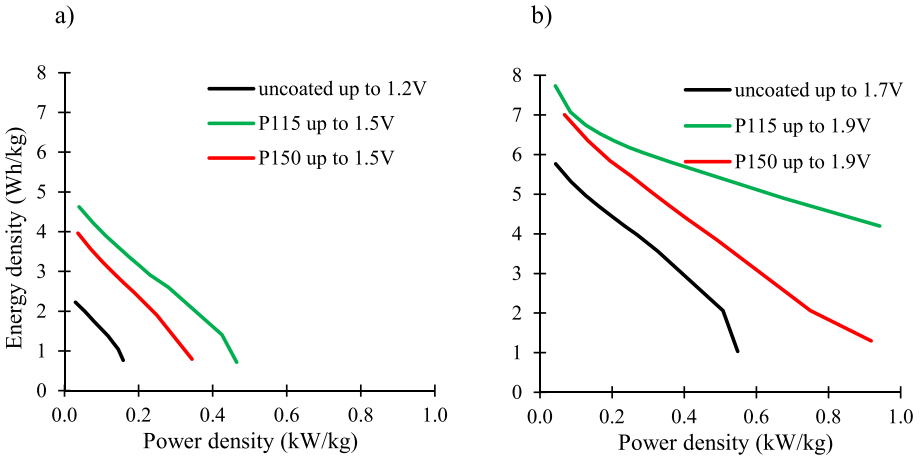


Fig. 10. Ragone plots obtained for cells fabricated with uncoated electrodes, with P115- and P150-coated electrodes. The cells were tested up to the voltage corresponding to a certain parasitic current density: 29 μA/cm^2 (a) and 47 μA/cm^2 (b).

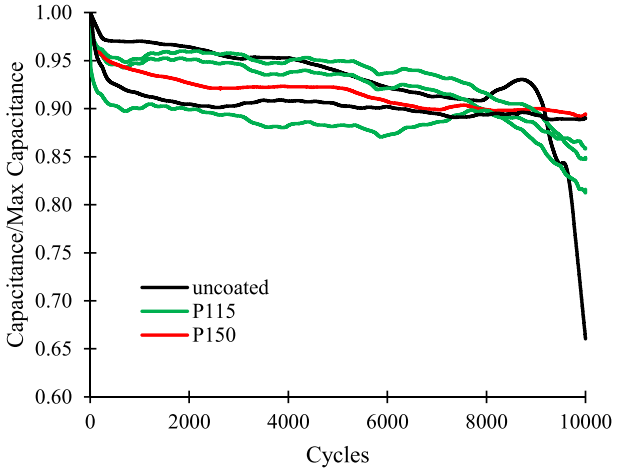


Fig. 11. Evolution of the ratio between the capacitance and the maximum capacitance of cells fabricated with uncoated electrodes, with electrodes coated at 1.15 V and with electrodes coated at 1.5 V during 10,000 cycles performed at 0.2 A/g between 0 and 1.9 V. The high frequency raw data were smoothed with a moving average of 500 elements.

a lower current density for a same potential - and the same current density for a higher potential – suggests a successful extension of the stable potential window. The capacitance also benefitted indirectly from this improvement, probably due to the mechanism of desolvation, which enables the access to more restricted pores at high potentials. As a result, the energy and power densities increased accordingly (e.g., for a 29 μA/cm^2 parasitic current density, they increased from 2.2 Wh/kg to 4.0 Wh/kg and to 4.6 Wh/kg and from 159 W/kg to 345 W/kg and to 465 W/kg, respectively). The long-term measurements suggest that the PPO-coating does not have a negative effect on the cyclability, but it also does not show a clear improvement when compared to cells fabricated with uncoated electrodes. A larger number of repeats are required to compensate the variability among the ageing profiles.

Supplementary data to this article can be found online at https://doi.org/10.1016/j.est.2022.104927.

CRediT authorship contribution statement

- J. M. Baptista: Conceptualisation, Methodology, Validation, Formal analysis, Investigation, Writing - Original draft, Visualisation
- G. Gaspar: Methodology, Investigation, Writing - Review & editing, Supervision
- K.G.U. Wijayantha: Conceptualisation, Resources, Writing - Review & editing, Supervision, Project administration, Funding acquisition
- K. Lobato: Writing - Conceptualisation, Resources, Writing - Review & editing, Supervision, Project administration, Funding acquisition.

Declaration of competing interest

The authors declare that they have no known competing financial interests or personal relationships that could have appeared to influence the work reported in this paper.

Acknowledgements

This work was funded by Fundação para a Ciência e a Tecnologia, I.P./MCTES through national funds (PIDDAC) –UIDB/50019/2020 and PD/BD/128169/2016. The authors also acknowledge the UK EPSRC JUICED Hub project EP/R023662/1 for the funding provided and Jagdeep Sagu, Jorge Correia, Filipe Serra and Daniel Santos for the fruitful discussions.

References

[1] X. Zang, C. Shen, M. Sanghadasa, L. Lin, High-voltage supercapacitors based on aqueous electrolytes, ChemElectroChem. (2018), https://doi.org/10.1002/celc.201801225.
[2] M. Sajjad, M.I. Khan, F. Cheng, W. Lu, A review on selection criteria of aqueous electrolytes performance evaluation for advanced asymmetric supercapacitors, J. Energy Storage 40 (2021), 102729, https://doi.org/10.1016/j.est.2021.102729.
[3] B. Pal, S. Yang, S. Ramesh, V. Thangadurai, R. Jose, Electrolyte selection for supercapacitive devices: a critical review, Nanoscale Adv. 1 (2019) 3807–3835, https://doi.org/10.1039/c9na00374f.
[4] Y. Liu, Q. Wu, L. Liu, P. Manasa, L. Kang, F. Ran, Vanadium nitride for aqueous supercapacitors: a topic review, J. Mater. Chem. A 8 (2020) 8218–8233, https://doi.org/10.1039/d0ta01490g.
[5] M. He, K. Fic, E. Frackowiak, P. Novák, E.J. Berg, Ageing phenomena in high-voltage aqueous supercapacitors investigated by *in situ* gas analysis, Energy Environ. Sci. 9 (2016) 623–633, https://doi.org/10.1039/c5ee02875b.
[6] Q. Gao, L. Demarconnay, E. Raymundo-Piñero, F. Béguin, Exploring the large voltage range of carbon/carbon supercapacitors in aqueous lithium sulfate electrolyte, Energy Environ. Sci. 5 (2012) 9611–9617, https://doi.org/10.1039/c2ee22284a.
[7] Y. Shao, M.F. El-Kady, J. Sun, Y. Li, Q. Zhang, M. Zhu, H. Wang, B. Dunn, R. B. Kaner, Design and mechanisms of asymmetric supercapacitors, Chem. Rev. 118 (2018) 9233–9280, https://doi.org/10.1021/acs.chemrev.8b00252.
[8] X. Wu, B. Huang, Q. Wang, Y. Wang, Wide potential and high energy density for an asymmetric aqueous supercapacitor, J. Mater. Chem. A 7 (2019) 19017–19025, https://doi.org/10.1039/c9ta06428a.
[9] L. Demarconnay, E. Raymundo-Piñero, F. Béguin, Adjustment of electrodes potential window in an asymmetric carbon/MnO 2 supercapacitor, J. Power Sources 196 (2011) 580–586, https://doi.org/10.1016/j.jpowsour.2010.06.013.
[10] S. Vaquero, J. Palma, M. Anderson, R. Marcilla, Mass-balancing of electrodes as a strategy to widen the operating voltage window of carbon/carbon supercapacitors in neutral aqueous electrolytes, Int. J. Electrochem. Sci. 8 (2013) 10293–10307.
[11] M. Yu, Z. Wang, H. Zhang, P. Zhang, T. Zhang, X. Lu, X. Feng, Amino functionalization optimizes potential distribution: a facile pathway towards high-energy carbon-based aqueous supercapacitors, Nano Energy 65 (2019), 103987, https://doi.org/10.1016/j.nanoen.2019.103987.
[12] M. Yu, D. Lin, H. Feng, Y. Zeng, Y. Tong, X. Lu, Boosting the energy density of carbon-based aqueous supercapacitors by optimizing the surface charge, AngewChemie 129 (2017) 5546–5551, https://doi.org/10.1002/ange.201701737.
[13] K. Fic, G. Lota, M. Meller, E. Frackowiak, Novel insight into neutral medium as electrolyte for high-voltage supercapacitors, Energy Environ. Sci. 5 (2012) 5842–5850, https://doi.org/10.1039/c1ee02262h.
[14] Y.Z. Wu, Y. Ding, T. Hayat, A. Alsaedi, S.Y. Dai, Enlarged working potential window for MnO_2 supercapacitors with neutral aqueous electrolytes, Appl. Surf. Sci. 459 (2018) 430–437, https://doi.org/10.1016/j.apsusc.2018.07.147.
[15] M.P. Bichat, E. Raymundo-Piñero, F. Béguin, High voltage supercapacitor built with seaweed carbons in neutral aqueous electrolyte, Carbon N. Y. 48 (2010) 4351–4361, https://doi.org/10.1016/j.carbon.2010.07.049.
[16] K. Fic, M. Meller, J. Menzel, E. Frackowiak, Around the thermodynamic limitations of supercapacitors operating in aqueous electrolytes, Electrochim. Acta 206 (2016) 496–503, https://doi.org/10.1016/j.electacta.2016.02.077.
[17] X. Wu, H. Yang, M. Yu, J. Liu, S. Li, Design principles of high-voltage aqueous supercapacitors, Mater. Today Energy 21 (2021), https://doi.org/10.1016/j.mtener.2021.100739.
[18] N. Dubouis, P. Lemaire, B. Mirvaux, E. Salager, M. Deschamps, A. Grimaud, The role of the hydrogen evolution reaction in the solid–electrolyte interphase formation mechanism for "Water-in-salt" electrolytes, Energy Environ. Sci. (2018) 3491–3499, https://doi.org/10.1039/C8EE02456A.
[19] L. Suo, O. Borodin, T. Gao, M. Olguin, J. Ho, X. Fan, C. Luo, C. Wang, K. Xu, "Water-in-salt" electrolyte enables high-voltage aqueous lithium-ion chemistries, Science 350 (6263) (2015) 938–943, https://doi.org/10.1126/science.aab1595.
[20] P. Lannelongue, R. Bouchal, E. Mourad, C. Bodin, M. Olarte, S. le Vot, F. Favier, O. Fontaine, "Water-in-salt" for supercapacitors: a compromise between voltage, power density, energy density and stability, J. Electrochem. Soc. 165 (2018) A657–A663, https://doi.org/10.1149/2.0951803jes.
[21] P.G. Kitz, P. Novák, E.J. Berg, Influence of water contamination on the SEI formation in Li-ion cells: an operando EQCM-D study, ACS Appl. Mater. Interfaces 12 (2020) 15934–15942, https://doi.org/10.1021/acsami.0c01642.
[22] C. Zu, H. Yu, H. Li, Enabling the thermal stability of solid electrolyte interphase in Li-ion battery, InfoMat. 3 (2021) 648–661, https://doi.org/10.1002/inf2.12190.
[23] S.S. Zhang, A review on electrolyte additives for lithium-ion batteries, J. Power Sources 162 (2006) 1379–1394, https://doi.org/10.1016/j.jpowsour.2006.07.074.
[24] Y. Lee, J. Chung, C. Jung, In-situ electropolymerization of linear acrylate monomers for the widening of supercapacitor operation potentials, Electrochim. Acta 253 (2017) 59–67, https://doi.org/10.1016/j.electacta.2017.09.004.
[25] S. Fletcher, V.J. Black, Poly(bisphenol) polymers as passivating agents for carbon electrodes in ionic liquids, J. Phys. Chem. C 120 (2016) 8014–8022, https://doi.org/10.1021/acs.jpcc.6b01725.
[26] W. Dong, T. Lin, J. Huang, Y. Wang, Z. Zhang, X. Wang, X. Yuan, J. Lin, I.-W. Chen, F. Huang, Electrodes with electrodeposited water-excluding polymer coating enable high-voltage aqueous supercapacitors, Research 2020 (2020) 1–13, https://doi.org/10.34133/2020/4178179.
[27] N. Jäckel, D. Weingarth, A. Schreiber, B. Krüner, M. Zeiger, A. Tolosa, M. Aslan, V. Presser, Performance evaluation of conductive additives for activated carbon

supercapacitors in organic electrolyte, Electrochim. Acta 191 (2016) 284–298, https://doi.org/10.1016/j.electacta.2016.01.065.
[28] S. Deheryan, D.J. Cott, R. Muller, M. Timmermans, M. Heyns, P.M. Vereecken, Self-limiting electropolymerization of ultrathin, pinhole-free poly(phenylene oxide) films on carbon nanosheets, Carbon N. Y. 88 (2015) 42–50, https://doi.org/10.1016/j.carbon.2015.02.059.
[29] S. Zeng, X. Shi, D. Zheng, C. Yao, F. Wang, W. Xu, X. Lu, Molten salt assisted synthesis of pitch derived carbon for Zn ion hybrid supercapacitors, Mater. Res. Bull. 135 (2021), 111134, https://doi.org/10.1016/j.materresbull.2020.111134.
[30] G. Feng, P.T. Cummings, Supercapacitor capacitance exhibits oscillatory behavior as a function of nanopore size, J. Phys. Chem. Lett. 2 (2011) 2859–2864, https://doi.org/10.1021/jz201312e.
[31] T. Xiong, H. Su, F. Yang, Q. Tan, P.B.S. Appadurai, A.A. Afuwape, K. Guo, Y. Huang, Z. Wang, M.S. Ji, T. Balogun, Harmonizing self-supportive VN/MoS_2 pseudocapacitance core-shell electrodes for boosting the areal capacity of lithium storage, Mater. Today Energy 17 (2020) 1–10, https://doi.org/10.1016/j.mtener.2020.100461.
[32] J. Duan, H. Hou, X. Liu, S. Liu, Q. Liao, Y. Yao, High performance PPO/Ti^{3+}/TiO_2NT membrane/electrode for lithium ion battery, Ceram. Int. 42 (2016) 16611–16618, https://doi.org/10.1016/j.ceramint.2016.07.082.
[33] J. Landoulsi, M.J. Genet, C. Richard, K. El Kirat, S. Pulvin, P.G. Rouxhet, Evolution of the passive film and organic constituents at the surface of stainless steel immersed in fresh water, J. Colloid Interface Sci. 318 (2008) 278–289, https://doi.org/10.1016/j.jcis.2007.09.087.
[34] X.R. Li, Y.H. Jiang, P.Z. Wang, Y. Mo, W. De Lai, Z.J. Li, R.J. Yu, Y.T. Du, X. R. Zhang, Y. Chen, Effect of the oxygen functional groups of activated carbon on its electrochemical performance for supercapacitors, Xinxing Tan Cailiao/New Carbon Mater. 35 (2020) 232–243, https://doi.org/10.1016/S1872-5805(20)60487-5.
[35] M.C. Burrell, J.J. Chera, Polyphenylene oxide (PPO) spin cast films by XPS, Surf. Sci. Spectra 6 (1999) 9–12, https://doi.org/10.1116/1.1247896.
[36] B. Xu, H. Wang, Q. Zhu, N. Sun, B. Anasori, L. Hu, F. Wang, Y. Guan, Y. Gogotsi, Reduced graphene oxide as a multi-functional conductive binder for supercapacitor electrodes, Energy Storage Mater. 12 (2018) 128–136, https://doi.org/10.1016/j.ensm.2017.12.006.
[37] T. Brousse, M. Toupin, D. Bélanger, A hybrid activated carbon-manganese dioxide capacitor using a mild aqueous electrolyte, J. Electrochem. Soc. 151 (2004) A614, https://doi.org/10.1149/1.1650835.
[38] E. Gileadi, E. Kirowa-Eisner, Some observations concerning the tafel equation and its relevance to charge transfer in corrosion, Corros. Sci. 47 (2005) 3068–3085, https://doi.org/10.1016/j.corsci.2005.05.044.
[39] K. Jurewicz, E. Frackowiak, F. Béguin, Towards the mechanism of electrochemical hydrogen storage in nanostructured carbon materials, Appl. Phys. A Mater. Sci. Process. 78 (2004) 981–987, https://doi.org/10.1007/s00339-003-2418-8.
[40] S. Wang, A. Lu, C.J. Zhong, Hydrogen production from water electrolysis: role of catalysts, Nano Converg. 8 (2021), https://doi.org/10.1186/s40580-021-00254-x.
[41] W.G. Nunes, B.G.A. Freitas, R.M. Beraldo, R.M. Filho, L.M. Da Silva, H. Zanin, A rational experimental approach to identify correctly the working voltage window of aqueous-based supercapacitors, Sci. Rep. 10 (2020) 1–9, https://doi.org/10.1038/s41598-020-75851-7.
[42] C. Prehal, C. Koczwara, N. Jäckel, A. Schreiber, M. Burian, H. Amenitsch, M. A. Hartmann, V. Presser, O. Paris, Quantification of ion confinement and desolvation in nanoporous carbon supercapacitors with modelling and *in situ* X-ray scattering, Nat. Energy 2 (2017), 16215, https://doi.org/10.1038/nenergy.2016.215.
[43] G. Li, T. Ouyang, T. Xiong, Z. Jiang, D. Adekoya, Y. Wu, Y. Huang, M.S. Jie, T. Balogun, All-carbon-frameworks enabled thick electrode with exceptional high-areal-capacity for Li-Ion storage, Carbon N. Y. 174 (2021) 1–9, https://doi.org/10.1016/j.carbon.2020.12.018.



https://dspace.org/

Electrodeposited poly(phenylene oxide) suppresses anodic parasitic processes in carbon-based supercapacitor electrodes operating in an aqueous electrolyte

Baptista, Joana M.; Gaspar, Guilherme; Wijayantha, Upul K. G.; Lobato, Killian

2022-06-02
Elsevier
https://doi.org/10.1016/j.est.2022.104927
Baptista JM, Gaspar G, Wijayantha KGU, Lobato K. (2022) Electrodeposited poly(phenylene oxide) suppresses anodic parasitic processes in carbon-based supercapacitor electrodes operating in an aqueous electrolyte. Journal of Energy Storage, Volume 52, Part B, August 2022, Article number 104927

Downloaded from a DSpace repository. https://dspace.org/